1. INTRODUCTION

Locating emission sources or hot spots of air pollutants is essential for many health and environmental reasons. To minimize the air pollutants' impact on the environment and the public health, it is necessary to identify the releasing sources properly and promptly so an effective control strategy could be implemented. For example, for homeland security applications, the release locations of harmful airborne contaminants usually are unknown. Their locations must be estimated from the post release concentration observations.[1] Another example is the leak detection of volatile organic compounds (VOCs) from the refinery or petrochemical industries. The American Petroleum Institute once estimated that >93% of reducible fugitive emissions came from 0.13% of the components (e.g. valves, connectors, flanges, etc) in process plants.[2] Detecting the possible leakages from thousands of components is always a challenging task; although fixing the identified leaking components not only protects the environment but also reduces the financial cost from unnecessary waste.

One way to identify the release or leakage locations is conducting a detailed survey by inspecting all the process components or potential locations one by one. This would require substantial investment in time, labor, and money. An alternative is setting up a matrix of point samplers in the field and create concentration contour plots by spatial interpolation algorithms (e.g. kriging) to identify the areas with high concentrations of pollutants. In Chen et al.,[3, 4] 3-hour canister samples were taken from 25 sites inside a petrochemical plant, twice per season for a year. These samples were then analyzed with gas chromatography-mass spectrometry according to the US EPA TO-14 method. A total of 19 emission sources were located from the contour maps of the VOCs measurements. The data collected from the sampling matrix also could be combined with air dispersion models for source localization. Conventionally, the dispersion models are used to predict downwind gas concentrations resulting from a known source. By <u>inverting</u> this process, the unknown gas source could be located from ambient measurements at multiple positions.[1, 5] Additional discussions on the inversion approach are given later.

The source localization methods mentioned above all relied on data collected with point samplers. Considering the required resources, usually only limited number of samplers can be deployed in the field. Their measurements are locally correct, but may not represent the overall situations. In addition, most of the collected samples provide only time-integrated information and are required to be sent back to the lab for further analysis. For example, a complete VOCs monitoring campaign with canisters may take more than a week, including canisters cleaning, sampling, GC/MS analysis, and data processing.[3] To protect the environment and human health, this kind of time lag between sampling and analysis is less desirable. Although currently there are several real-time monitoring devices (such as electrochemical sensors and surface acoustic wave sensors) that can provide real-time information about the airborne chemicals' concentrations *in situ*, they usually monitor only certain type of chemicals. Each chemical needs a specific type of detector. In

other words, prior knowledge about the properties of the chemical to be detected is required. Unfortunately, this kind of information is not readily available most of the time.

In this project, we proposed using optical remote sensing techniques to overcome some of the limitations associated with the point samplers. More specifically, we focused on the Open-Path Fourier Transform Infrared (OP-FTIR) spectroscopy. The OP-FTIR can provide real-time information *in situ* for mixtures of air pollutants and scan a much larger area than the point samplers to get spatially representative data. Based on computer simulated and field collected data, we developed and evaluated three source localization approaches with the OP-FTIR spectroscopy: (1) one-dimensional radial plume mapping; (2) two-dimensional radial plume mapping; (3) inversing dispersion models.

2. ONE-DIMENSIONAL RADIAL PLUME MAPPING

One possible approach for locating these sources is placing multiple point samplers (e.g., canisters) and analyzing the samples in laboratories. The sources then could be identified by mapping the concentration distributions using geostatistical techniques.[6, 4] Due to the potential time lag between field campaigns and obtaining the results of chemical analyses, this approach may not be suitable for situations when getting prompt answers is desired. Another limitation is the fact that sometimes it may not be feasible to place the sampling devices directly in areas with potential emission sources because of the objection of the property owners.

One alternative approach, i.e., one-dimensional radial plume mapping (RPM_{1D}) developed by Hashmonay and Yost,[7] is based on ground-based optical remote sensing (ORS) techniques. Most ORS instruments, such as Open-Path Fourier Transform Infrared Spectroscopy [8, 9] and Ultra-Violet Differential Optical Spectroscopy, [10, 11] can identify and quantify multiple air pollutants in near real-time.[12] The RPM_{1D} approach involves deploying an ORS instrument at a downwind location and collecting path-integrated concentration (PIC) data of multiple beam paths along a 1D scanning beam geometry. The upwind source locations can be estimated by combing the information on wind direction and the distribution of the plume reconstructed from the PIC data. Two tracer gas experiments demonstrated that this approach provided reasonable results for estimating source locations.[7, 13] The guideline for conducting such measurements is provided in the 'Other Test Method 10' (OTM-10)[14] published by the US EPA.

Observations from previous field studies showed that the uncertainty in the results of locating the sources using the RPM_{1D} approach tends to have certain levels of directionality. For example, in Wu et al.,[13] the estimated source locations spread along the major wind directions even though the distance from the regression line of these estimated results to the true source location was only 10 m (approximately 10% of the 97 m beam path). In the current study, we propose setting up an additional monitoring line that runs perpendicular to the original 1D scanning beam geometry to reduce this uncertainty. We conducted a series of simulation studies and a proof-of-concept field experiment to evaluate the validity and feasibility of the proposed approach.

2.1 MATERIALS AND METHODS

Simulation Investigation

In the simulation study, a series of air pollution plumes was generated using a Gaussian dispersion model at multiple source locations under various meteorological conditions. The size of the spatial domain used for evaluation was assumed to be 201 m by 201 m (Figure 2.1). This domain was divided into 20 x 20 square pixels (10 m each side). For each simulation scenario, a point source was assumed to be at the center of one of these pixels; therefore, a total of 400 point source locations were simulated. The ORS instrument was at the coordinate of (0, 0) with two 1D scanning lines

running perpendicular to each other. Each monitoring line had three retroreflectors creating three segments of equal distance (67 m) for the plume reconstructions. This setup was identical to the one used in the subsequent field study.

Simulation of Downwind Plume Distributions and PIC

For each source location, the Gaussian dispersion model used to simulate the downwind concentrations of the plumes along the two monitoring lines was expressed as [15]

$$\chi(x, y, z : H) = \frac{Q}{2\pi u \sigma_y \sigma_z} \exp\left[-\frac{y^2}{2\sigma_y^2}\right] \left\{ \exp\left[-\frac{(H-z)^2}{2\sigma_z^2}\right] + \exp\left[-\frac{(H+z)^2}{2\sigma_z^2}\right] \right\}$$
(2.1)

where χ is the air pollutant concentration at the downwind receptor (x, y, z) in the Cartesian coordinate system; Q is the pollutant emission rate; u is the wind speed; H is the effective height of the plume; and (σ_y and σ_z) are the standard deviations of the concentration distributions in the crosswind and vertical directions, respectively. In this study, we assumed z=0 and H=0. The flow rate was fixed at 10 L/min because our preliminary study showed that this provided detectable plumes at the ORS monitoring lines.

At each monitoring line, the wind direction varied within ±45° from the perpendicular to the monitoring line with an increment of 1° (i.e., 315° to 45° for the X monitoring line and 45° to 135° for the Y monitoring line). The observed PIC (PIC_{obs}) of each beam path at a certain wind direction was simulated by numerically integrating the simulated plume's distribution along the monitoring line from zero to each of the corresponding retroreflectors. The three PIC_{obs} (i.e., one for each beam path) were defined as a set of PIC_{obs}.

Source locating

The first step in locating the sources was to reconstruct the peak locations of the plume along the 1D monitoring line using the smooth basis function minimization (SBFM) approach. The SBFM fits the distribution functions to satisfy the input beam integrals (i.e., the PIC_{obs}). In the fitting procedure, a Gaussian distribution was chosen as the basis function, as in most of the previous studies. The error function for minimization was defined as the sum of squared errors between the observed and predicted PIC (PIC_{pred}). The latter term is given as follows:[13]

$$PIC_{pred,i}(p_{jk}) = \sum_k \int_0^{Li} G_k(x; p_{jk}) dx$$
(2.2)

where j is the parameter number index; k is the basis function number index; L_i is the ith beam path length; p_{jk} is the jth parameter of the kth basis function; and G_k is the kth basis function. In this study, k equaled 1 (one basis function), j equaled 2 (peak location and standard deviation of the assumed Gaussian distribution), and i ranged from 1 to 3 (three beam paths at each monitoring line). The

minimization procedure was implemented by using the "lsqnonlin" function in the MATLAB software (MathWorks, Inc., Natick, MA). For each reconstruction, the input data was the PIC_{obs} set and the output was the parameters of the basis functions (p_{jk}) in Equation 2.

The second step in locating the sources involved calculating the line equations from the reconstructed peak locations (i.e., points) and their corresponding wind direction information (i.e., slopes). The source locations (or the intersection points) were then estimated by solving every two line equations simultaneously. The estimated results were categorized into three groups according to whether data from one or two monitoring lines were used. The first two groups contained the results from using the reconstructed peak locations at only one of the monitoring lines, i.e., either the X monitoring line or Y monitoring line, as was the case in the original one-line RPM_{1D} technique. These two approaches were called $X-RPM_{1D}$ and $Y-RPM_{1D}$, respectively. For each simulated source location in these two groups, there were 4095 ($= C_2^{91}$) intersection points as having 91 different wind directions at each monitoring line. The third group contained the results from using the reconstructed peak locations at both monitoring lines, i.e., one at the X monitoring line and the other at the Y monitoring line, as was the case for the proposed two-line RPM_{1D} approach ($XY-RPM_{1D}$) of this study. The number of intersection points for each source location in this group was 8281 (=91x91).

The performance of the source locating results was evaluated mainly based on the following two measures. First, the distance (DIST) between the real source location and the center of the grid with the highest density of intersection points was calculated to represent the accuracy of the locating results. Second, the area of the grids with >50% ($AREA_{50\%}$) or >25% ($AREA_{25\%}$) relative frequency of occurrence (which was standardized by the highest occurring frequency among the locating results) was calculated to represent the uncertainty of the locating results. Because the Gaussian dispersion model is generally applied for estimating concentrations at receptors more than 100 m from a source,[16] we focused on the results for sources located between (100,100) to (200, 200) (called the 'main domain') in the overall domain.

Field study

Data Collection

The field study was conducted in an open space with the same OP-FTIR scanning geometry as the one used in the simulation study (Figure 2.1). The OP-FTIR (OP-300B, Mastek Technologies, Inc, Taipei, Taiwan), which was mounted on a custom-built stepper motor and equipped with a mercury cadmium telluride (MCT) detector, was located at the origin. Three retroreflectors were set up along each of the two monitoring lines. The optical centerline was at a height of approximately 1.4 m. A meteorological station, collecting wind data at a temporal resolution of 1 sec, was set up near the monitoring line.

Sulfur hexafluoride (SF_6) was released at the coordinate of (100, 100) as a tracer gas with the

flow rate set at 10 L/min. The release system was composed of 5 porous tubes (diameter = 5 mm), and its dimension was approximately 1 m × 1 m. When the trace gas was released, the OP-FTIR scanned the retroreflectors from 1 to 6 sequentially and repeatedly. A complete scan of the 6 beams took approximately 5.5 minutes, including 42 seconds to collect one spectrum and 5 to 35 seconds to move the IR beam from one retroreflector to the next. A total of 133 complete scans were collected.

Data Analysis

The collected spectra were quantified using the classical least squares method to obtain the PIC_{obs} (in ppm-m). The quantification region for SF_6 was from 935 to 955 cm^{-1}.[17] Because the wind data were collected at a higher temporal resolution than for the OP-FTIR spectra, their mean values were calculated to match the corresponding collection period of each PIC_{obs} set. We further applied a moving average scheme with a group size of 2 on the PIC_{obs} and wind data to reduce errors resulting from temporal variability.[14] The SBFM algorithm was implemented on these moving average values to obtain the peak locations at the downwind monitoring lines. Using the one-line or two-line RPM_{1D} approach, we estimated the source locations from the wind data and the reconstructed peak locations.

The following screening criteria were implemented to improve the source locating results. (1) The Concordance Correlation Factor between the measured and predicted PIC (CCF_{PIC}), which is similar to the Pearson correlation coefficient with adjustments for the shifts in location and scale,[14] was calculated to represent the goodness of fit during the SBFM reconstruction. We excluded the peak reconstruction results with a CCF_{PIC} below 0.7. (2) A large variation in wind direction when collecting each PIC_{obs} set gave additional errors because the three beam paths were not scanned simultaneously. Therefore, we eliminated the peak reconstruction results if the corresponding standard deviation (SD) of wind directions was larger than 20°. (3) Previous studies have shown that the SBFM algorithm might not reconstruct the peak locations accurately when the downwind concentrations congregated within a certain segment of the beam path.[13] We eliminated the data set if one of the PIC_{obs} segments (i.e., the difference between two adjacent PIC_{obs}) was higher than 90% of the largest PIC_{obs}. (4) When calculating the intersection points from the line equations, having two wind directions that were too close to each other (i.e., similar slopes) would give a solution that was unreasonably far away from the experimental domain. We excluded the estimated source locations if the angle between the paired wind directions was less than 5°.[13]

2.2 RESULTS AND DISCUSSION

Simulation Study

Figure 2.2 shows the locating results from using the X-, Y-, and XY-RPM_{1D} approaches at three example source locations at (100, 100), (150, 100), and (150, 150). As observed in previous studies, the uncertainty of the estimated source locations was distributed quite perpendicularly to the monitoring line when the one-line RPM_{1D} approach was applied (Figure 2.2, Column 1: X-RPM_{1D};

Column 2: Y-RPM$_{1D}$). This directionality was reduced using the XY-RPM$_{1D}$ approach (Figure 2.2, Column 3). The uncertainty area of this approach resembles the joint distribution of the directional uncertainty distributions from the X- and Y-RPM$_{1D}$ approaches. These effects were also observed after adding 30% of noise to the simulated PIC$_{obs}$ and recalculating the source locations.

With regard to the accuracy of the locating results, the DIST values were the smallest when using the XY-RPM$_{1D}$ approach for the sources at (100,100) and (150, 150) (=1.41 and 4.24, respectively, Figure 2.2). However, the Y-RPM$_{1D}$ approach yielded the smallest DIST value (=0 m) for the source at (150, 100). The reason for the relatively worse results from the other two approaches is that this location is closer to the boundary of the X-axis but at the center of the Y-axis. Therefore, the plumes tended to spread over the OP-FTIR scanning domain on the X-axis under certain wind directions. One such example is given in Figure 2.3, in which the wind direction was 334$^{\mathrm{o}}$, and the peak location of the downwind plume was at 198 m. The SBFM gave a biased estimate of the peak location (=191m) under this condition, which consequently affected the source locating results when solving the line equations. This explains why the DIST value was largest when using the X-RPM$_{1D}$ approach at this location. However, by adding the data collected along the Y-axis (where downwind plumes mostly refined within the OP-FTIR scanning domain), the XY-RPM$_{1D}$ approach decreased the DIST value to 3.00 m. The above explanation is also applicable for the worse results found at location (150,150) than at (100,100) when comparing within the same reconstruction approach (Figure 2.2, Row 3 vs. Row 1).

For the 100 source locations in the main domain, the DIST values calculated from the three RPM$_{1D}$ approaches are shown in Figure 2.4. The percentage of locations with a DIST less than 40 m (i.e., 20% of the longest beam path, a validation index suggested in the OTM-10) was 47.9% from both X- and Y-RPM$_{1D}$. However, it was 100% from XY-RPM$_{1D}$, indicating that using information from both monitoring lines gave acceptable results regardless of the true source locations. The average DIST value was 3.7 m, compared to that of 81.6 m from the other two approaches. For the 400 simulated source locations in the overall domain, the percentage of those with DIST less than 40 m from XY-RPM$_{1D}$ decreased slightly to 89.0%.

As demonstrated in Figure 2.2 (Row 2), the two-line RPM$_{1D}$ approach did not necessarily yield better results than the one-line RPM$_{1D}$ approaches. We further calculated the difference between the first and second largest DIST values from the three reconstructed approaches at each source location. The results showed that the XY-RPM$_{1D}$ performed better than the other two approaches at 68.6% of the source locations in the main domain. At locations where it did not provide better results, the average difference was only 2.2 m (range: 0.4 to 4 m). This indicated that even though using two-line RPM$_{1D}$ did not give the most accurate results at all the locations, the difference was almost negligible.

The uncertainty of the locating results at the three example locations is given in Table 1. There

was no clear trend at the 50% uncertainty levels, but the two-line RPM_{1D} approach provided consistently smaller AREA values at the 25% uncertainty level. In the sensitivity analysis, we added 30% noise to the input PIC_{obs} values and this trend was even more apparent (Table 2.1). Among all of the simulated source locations, the mean $AREA_{50\%}$ was 10.4 m^2 and 6.5 m^2 by using one- and two-line RPM_{1D}, respectively, when limited to locations with good precisions of DIST<40 m. The corresponding mean $AREA_{25\%}$ was 40.8 m^2 and 22.2 m^2, respectively.

Field study

The average wind speed was 3.1 m/s in the field study within the preferred range of 1 to 8 m/s, as suggested in OTM-10. The wind mainly originated from the northeast direction in the field study (Figure 2.1). The standard deviation of the wind direction within each PIC_{obs} set ranged between 5.7° to 55.7°, which was relatively large compared to the value found in a previous study (=10°).[13] The detection limit of PIC_{obs} collected in the field study ranged between 0.02 to 0.08 ppm-m, and measurements below the detection limit were set as 0. The mean PIC_{obs} was 1.7 ppm-m with a standard deviation of 2.3 ppm-m. The PIC sets with all three PIC_{obs} at 0 were not included in the following SBFM reconstruction because they provided limited information about the distributions of the plumes.

In the SBFM reconstruction process, the original mean CCF_{PIC} was 0.66 and 0.71 based on data collected in the X- and Y-monitoring lines, respectively. After applying the screening criteria, the number of PIC_{obs} sets available for locating the sources was 18 and 42 for the two monitoring lines, respectively, and the CCF_{PIC} ranged between 0.83 and 1. The estimated source locations are shown in Figure 2.5 (Row 1), and the grayscale bar represents the relative frequency of occurrence of these locations. Due to the small number of input PIC sets and the resulting intersection points, regions with a high relative frequency of occurrence were difficult to observe directly in the plots and did not actually cover the true source location. The DIST values ranged between 28.4 and 53.5 m. Several efforts were made to improve the results. First, a spatial averaging filter with a filter size of 5 m-by-5 m was implemented.[18] The source locations in the resulting plots were much more discernible (Figure 2.5, Row 2). Second, an uncertainty analysis based on the Monte Carlo method[19] was incorporated in the source locating process by resampling the peak locations randomly 300 times within the range of the SBFM reconstructed value ± 10 m for each PIC_{obs} set and then solving the line equations.[13] Thus the number of intersection points (Figure 2.5, Row 3) was 300 times higher than the original number of solutions. Third, we kept only the results when the corresponding wind direction was within ±45° perpendicular to the monitoring lines (Figure 2.5, Row 4). The final DIST and $AREA_{25\%}$ were the smallest using the two-line RPM_{1D} approach (=18.4 m and 4697 m^2) compared to the 29.0-62.2 m and 5561-5792 m^2 from the one-line RPM_{1D} approaches.

Although previous studies have demonstrated the utility of the one-line RPM_{1D} approach, we found that its performance was less than ideal, especially for the X monitoring line in the current

study. Possible explanations are given as follows. Due to the physical restrictions of the experimental site, we could not set up the beam geometry such that the wind direction was mostly perpendicular to either of the monitoring lines. This posed a special challenge for the RPM_{1D} algorithm because the plumes could spread beyond the 1D scanning domain. This was evidenced by the fact that approximately half of the reconstructed peaks located at the first beam segment closest to the OP-FTIR in the field study. Another challenge was the large variation of the wind direction in our study. Due to this, the distribution of the plumes might vary significantly within the data collection periods of each PIC_{obs} set. We attempted to minimize this effect by implementing the data screening criteria of eliminating the peak reconstruction results with a SD of wind direction larger than 20° or a CCF_{PIC} below 0.7. These procedures unavoidably reduced the PIC_{obs} sets available for locating the sources. Only 15 sets of PIC_{obs} were left for the SBFM reconstruction along the X-axis, leading to a source estimation plot with a sparse density (Figure 2.5j). For the $Y-RPM_{1D}$ approach, 39 sets of PIC_{obs} were available for the SBFM reconstruction, and the actual source location was near the boundary of the 0.25-probability area (Figure 2.5k). Our proposed $XY-RPM_{1D}$ approach gave improved results under these unfavorable but realistic test conditions. The real source location was close to the boundary of the 0.5-probability area (Figure 2.5l). The DIST value was less than 20 m, and the $AREA_{25\%}$ was reduced by 16% to 19% (i.e., from 5561-5792 m^2 of the one-line RPM_{1D} approaches to 4697 m^2).

The current study design of having the OP-FTIR scan from Retro 1 to Retro 6 sequentially and repeatedly was not optimal. During the period when, for example, the northern wind prevailed, the OP-FTIR was still programmed to scan along the Y-axis, which unavoidably reduced the usable number of PIC_{obs} sets on the X-axis. One potential way to overcome this limitation is designing a 'smart' OP-FTIR scanning procedure by determining the scanning beam paths in real-time based on the on-site wind direction data.

2.4 SUMMARY

The simulation study demonstrated that using the proposed two-line RPM_{1D} approach gave better results (i.e., smaller DIST values and uncertainty areas) than the original one-line RPM_{1D} approach at most simulated source locations. The DIST values in the main domain were all smaller than 40 m with a mean of 3.7 m. In the field study, this approach gave reasonable results even under unfavorable test conditions of unstable wind directions, wind blowing toward the OP-FTIR, and a small number of PIC_{obs} sets on one axis. The DIST was 18.4 m (9.2% of the longest beam path), and the $AREA_{25\%}$ was 4697 m^2 (11.6% of the studied domain). For future application of this technique, we recommend using the results obtained from the RPM_{1D} approach to refine the potential source regions followed by detailed surveys with conventional point samplers. In the current study, we focused on the scenarios of ground sources in open space. The performance of both the one-line and two-line RPM_{1D} approaches for elevated sources and complex terrain requires further investigation.

Table 2.1. Uncertainty of the source locating results at three example locations in the simulation studies.

| Source location | Added noise%[1] | X-RPM$_{1D}$ | | Y-RPM$_{1D}$ | | XY-RPM$_{1D}$ | |
		AREA$_{50\%}$[2]	AREA$_{25\%}$[3]	AREA$_{50\%}$[2]	AREA$_{25\%}$[3]	AREA$_{50\%}$[2]	AREA$_{25\%}$[3]
(100, 100)	0	10	29	10	29	13	27
	30	16	63	11	65	11	34
(150, 100)	0	4	30	10	20	6	12
	30	28	184	30	197	4	26
(150, 150)	0	4	29	4	29	3	18
	30	13	88	22	79	11	53

[1]Noise% added to the simulated path integrated concentrations.

[2]Area (m^2) of the grids with >50% relative frequency of occurrence after implementing the same data screening criteria as in the field experiment.

[3]Area (m^2) of the grids with >25% relative frequency of occurrence after implementing the same data screening criteria as in the field experiment.
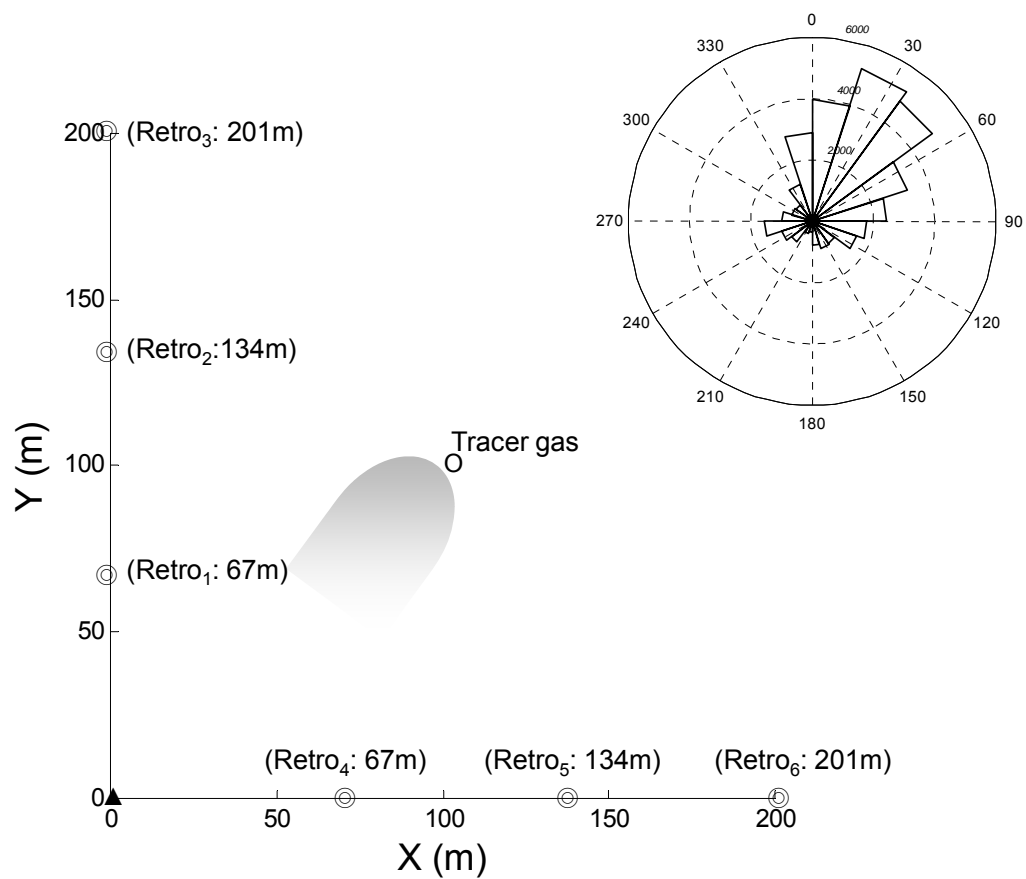
Figure 2.1. Plan view of the experimental setup. The inserted angle histogram plot represents the wind directions in the field study. ▲: optical remote sensing instrument; ◎: retroreflector; o: release location in the field experiment.
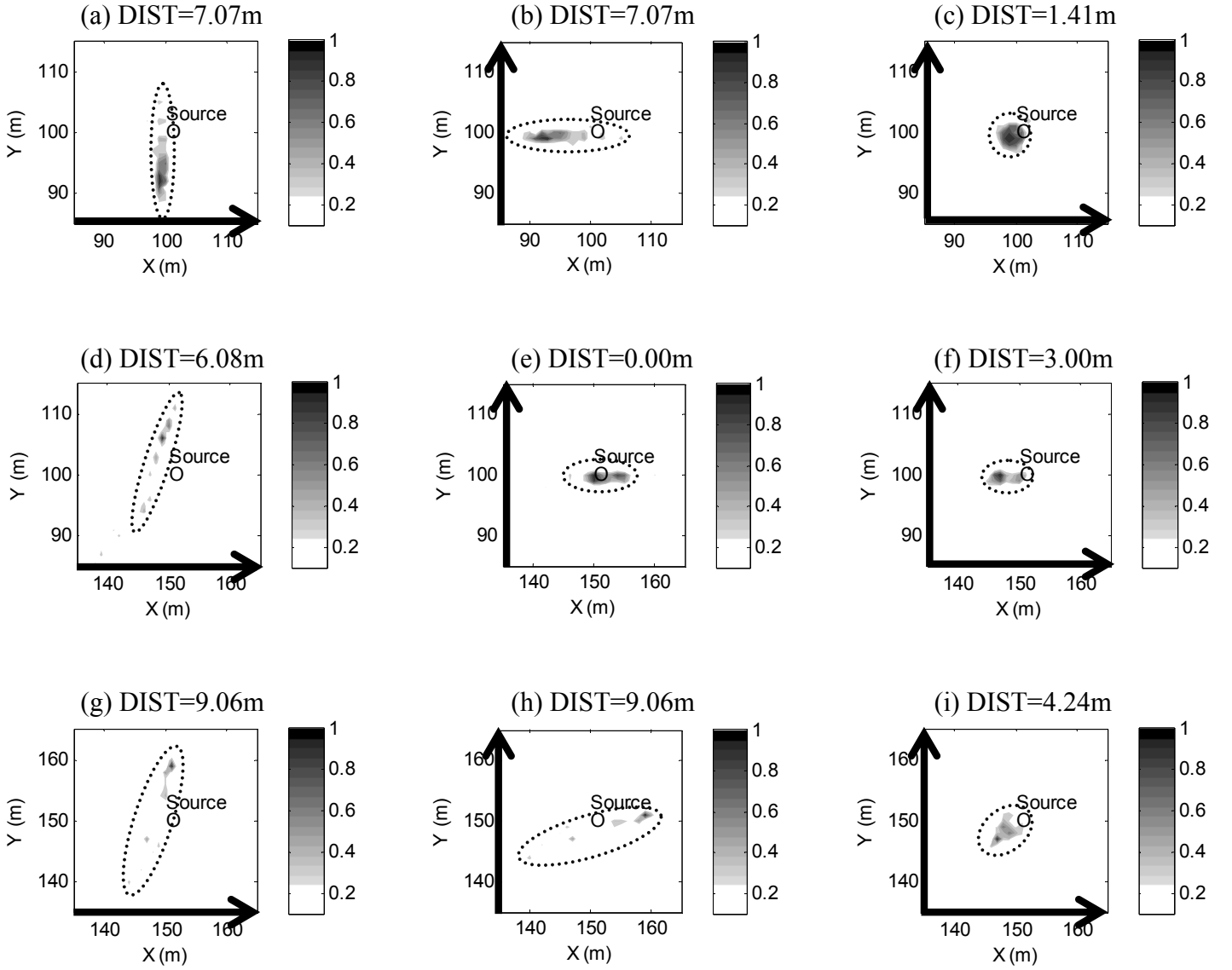
Figure 2.2. Reconstruction results at three example source locations in the simulation studies. The grayscale bar represents their relative frequency of occurrence. Rows 1 to 3: Source at (100, 100), (150, 100), and (150, 150), respectively. Columns 1 to 3: Reconstructed by the X-RPM$_{1D}$, Y-RPM$_{1D}$, and XY-RPM$_{1D}$ approaches, respectively.
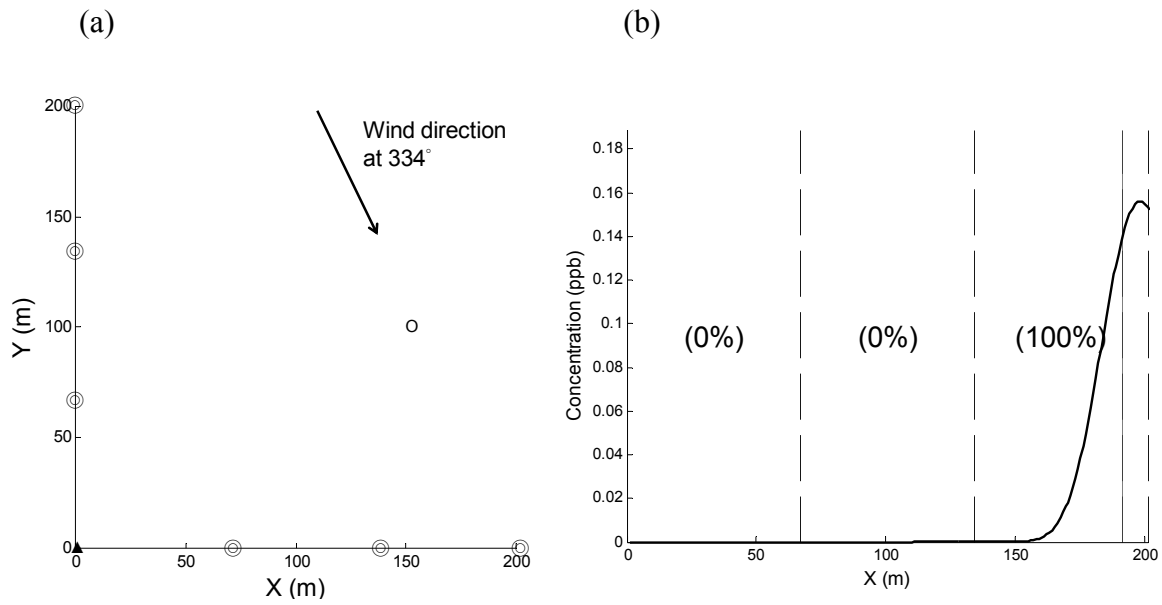
Figure 2.3. Example of a simulated plume spreading over the scanning domain on the X-axis. (a) The simulated beam geometry and source location (o). ▲: optical remote sensing instrument; ◎: retroreflector. (b) The simulated downwind plume distribution along the X-axis. The dotted vertical lines represent the locations of the three retroreflectors and the solid vertical line represents the reconstructed peak location. The values in parenthesis present the percentage of each PIC segment compared to the total PIC.
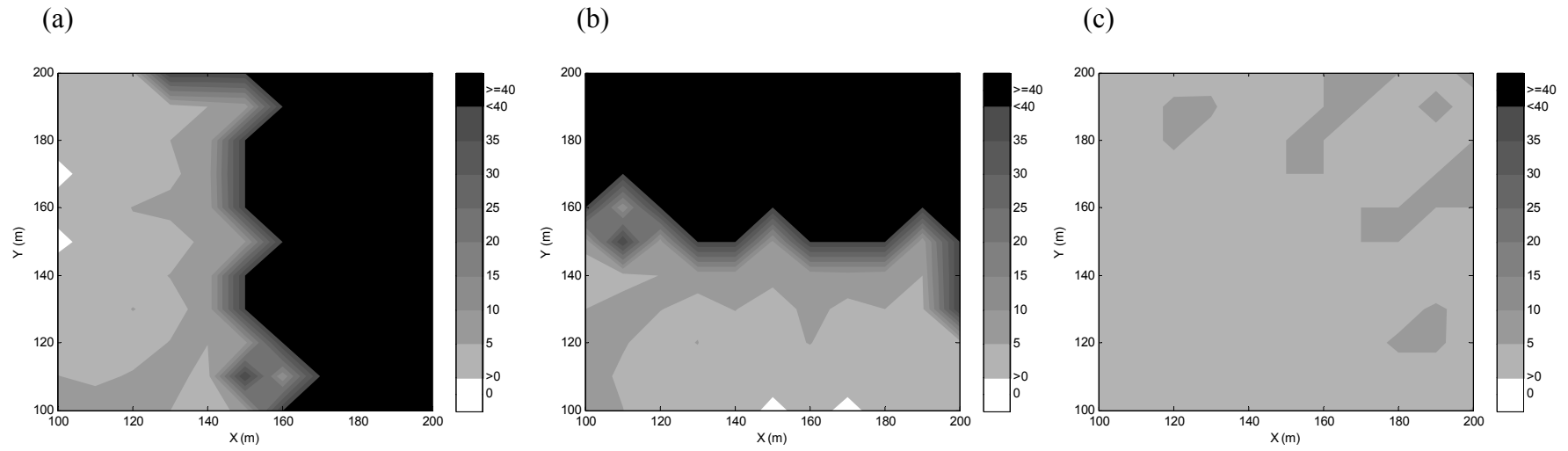
Figure 2.4. Error maps of the simulation results within the main domain. The grayscale bars represent the DIST values at each simulated source locations by using the (a) X-RPM$_{1D}$ approach; (b) Y-RPM$_{1D}$ approach; and (c) XY-RPM$_{1D}$ approach.
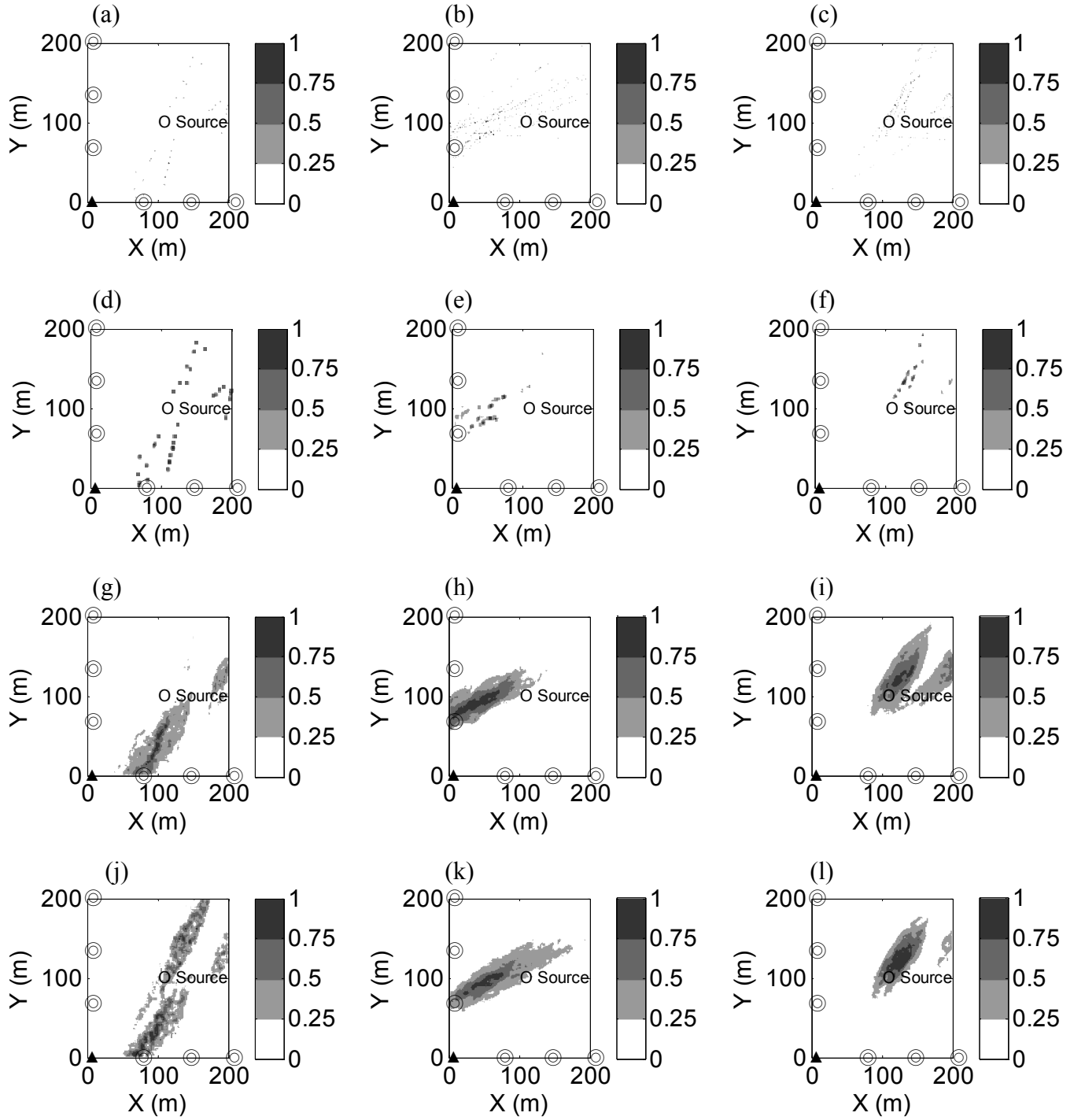
Figure 2.5. Reconstruction results in the field experiment. The grayscale bar represents their relative frequency of occurrence. Columns 1 to 3: Reconstructed by the X-RPM$_{1D}$, Y-RPM$_{1D}$, and XY-RPM$_{1D}$ approaches, respectively. Row 1: Original estimates. Row 2: After implementing a spatial averaging filter with a filter size of 5m-by-5m. Row 3: After the uncertainty analysis by resampling reconstructed peak locations 300 times. Row 4: After keeping only the results when the corresponding wind direction was within ±45° perpendicular to the monitoring lines.

3. TWO-DIMENSIONAL RADIAL PLUME MAPPING

Several researchers have applied optical remote sensing (ORS) instruments with the computed tomography (CT) technique to locate the pollution sources in a timely fashion.[20, 21] However, the involvement of complicated CT beam geometry composed of more than one ORS instrument or multiple detectors limited its real-world application.[22, 23] A novel radial plume mapping (RPM) technique using only one ORS instrument with multiple retroreflectors was proposed for further improvement in this field. The US EPA 'Other Test Method 10' (OTM-10),[14] which was released in 2006, provided the guidelines for conducting RPM measurements. The horizontal radial plume mapping (HRPM) technique described in the OTM-10 was designed to locate hot spots of air contaminants. In previous studies, this technique was evaluated with both computational simulation approaches[24, 25] and field experiments.[26, 25] For example, in Hashmonay et al.,[25] the author demonstrated that the HRPM technique was able to give comparable results for plume characterization to the CT technique. In our previous study,[17] we further evaluated the performance difference between two reconstruction algorithms that were commonly used in the HRPM technique.

What is less known is the feasibility of using the HRPM technique for identifying multiple plumes of the same substance. In this study, we evaluate the performance of the HRPM technique to locate two plumes with computational simulation data. A series of test maps with two plumes along with the associated path integrated concentration (PIC) data were simulated. These PIC data were then reconstructed by the HRPM technique to estimate the peak locations. Several modifications were also proposed to improve this technique.

3.1 MATERIALS AND METHODS

Generation of Test Maps and Associated PIC

The study domain was set at 30×30 dimensionless units and was further divided into nine pixels of equal size. A nine-beam geometry was assumed to have one ORS instrument at the origin and the path-defining components (e.g., retroreflectors) on the edge of each pixel such that the beam paths passed through the center of each pixel (Figure 3.1a). This was to maximize the beam path length within each pixel and minimize the error magnification of the algorithm.[27] Two symmetric Gaussian distributions with the same height, width (standard deviation, SD=2), and shape were generated with the peak locations at the center of different pixels to form one test map. Thus, the total number of the test maps in this series was 36 ($= C_2^9$). Another series of test maps (n=36) were generated with larger SD (=4) at the same locations. Previous studies also used the Gaussian distributions to generate the test maps[22, 28] and thus allowed the researchers to directly compare the input parameters to the parameters obtained from the reconstructed algorithm.[24] The observed PIC (PIC$_{obs}$) of the nine beam paths were calculated by integrating the simulated Gaussian distributions and were defined as follows:

$$PIC_{obs,i}\left(P_{jk}\right)=\sum_{k}\int_{0}^{L_i}G_k(x;p_{jk})dx \quad ,$$
(3.1)

where j is the parameter number index, k is the basis function number index, L_i is the ith beam path length, p_{jk} is the jth parameter of the kth basis function, and G_k is the kth basis function. For this study, k equaled 2 (two basis functions, which are both Gaussian distributions), and i ranged from 1 to 9 (nine beam paths). To simplify the test map, we incorporated two identical bivariate Gaussian distributions with the same standard deviation in both the x-axis and y-axis to generate the test map. Furthermore, the correlation between the x and y components of both Gaussian distributions were set at 0, and thus, j equaled 4 (i.e., the peak location at x, y, standard deviation, and scaling factor for the peak height).

In real-world applications, it takes time for the ORS instrument to scan from one retroreflector to another. Because the PICs are not collected simultaneously and the plumes might fluctuate as the meteorological condition changes, it was essential to investigate the reconstruction stability of the NNLS algorithm. Thus, for the sensitivity analysis, we added random errors of 1, 5, 10, 20, and 30 percent to each PIC set (defined as PICs for Path 1 to 9), and thus, 180 additional PIC sets were generated (36 × 5) for each map series. For example, the random error within 1 percent of the original PIC_{obs} was added to all the synthetic PIC_{obs} data derived from the 36 test maps. The NNLS algorithm was then performed to reconstruct all the 36 maps.

NNLS Reconstruction

NNLS is an iterative algebraic deconvolution algorithm. The observed PIC for deconvolution to retrieve the concentration information is given by:

$$PIC_{obs,k}=\sum_{k}K_{km}c_m \quad ,$$
(3.2)

where K is the kernel matrix that incorporates the specific beam geometry, k is the number index of the beam paths, m is the number index of the pixels, and c_m is the concentration in the mth pixel. In this study, k and m both equaled 9 (nine beam paths and nine pixels). Each element in the kernel matrix represents the length of the kth beam path in the mth pixel. Given PIC_{obs} and K_{km} in Equation 2, the NNLS was able to solve for c_m. The geostatistical method of kriging was further applied to generate a smooth surface map and to avoid limiting the peak in the center of each pixel.

Evaluation of the Reconstruction Quality

Three indicators were used to evaluate the reconstruction quality. First, the concordance correlation factor between the observed and reconstructed PIC (CCF_{PIC}) was calculated to describe the quality of fit between them and to determine whether the solution search process was optimized. The CCF is similar to the Pearson correlation coefficient, with adjustments for the shifts in location

and scale. A CCF equal to 1 represents a perfect match between the two sets of data. Second, a successful reconstruction result was defined as having the peak locations of both underlying Gaussian plumes covered by regions with a relative concentration above 0.5 ($CONC_{E50\%}$) in the reconstructed maps. The relative concentrations were calculated by standardizing the reconstructed results with the highest concentration among each map so that the maximum was 1. The last indicator was the area of the $CONC_{E50\%}$, which was used to describe the uncertainty of the reconstruction results.

3.2 RESULTS AND DISCUSSION

One example of the test distributions (SD=2) and the reconstructed results is given in Figures 3.1b and 3.1c. Both test plumes were away from the origin (in Pixels G and I). The CCF_{PIC} was 1, indicating that it obtained the converged solution. The NNLS algorithm gave reasonably good estimates of the source locations. The area of $CONC_{E50\%}$ was 138.3 square units (15.4% of the studied area) and covered both real source locations. Similar results were also observed for the wide plumes (SD=4, Figures 3.1d and 3.1e). The area of $CONC_{E50\%}$ was 187.3 square units and covered both real source locations. The overall reconstruction results for the test maps with SD=2 are given in Table 3.1. The high CCF_{PIC} values for both the successful and failed cases (0.93±0.08 and 0.94±0.05, respectively) indicated that the NNLS algorithm successfully found converged results. Among the 36 test maps, 32 of them were with the $CONC_{E50\%}$ covering both plumes (success rate=89%), and the average area for successful reconstructions was 174.0±24.5 square units (<20% of the studied area). Better performance was observed for the large plumes. The $CONC_{E50\%}$ covered both peak locations in all test maps (success rate=100%) and the average area of $CONC_{E50\%}$ was 204.6±20.6 square units (22% of the studied area). Note that the area statistics obtained from the plumes with different sizes (i.e., SD=2 vs. 4) should not be compared directly since a wider plume naturally yields a larger area of $CONC_{E50\%}$.

Figure 3.2 shows examples of two plumes in proximity of each other. Although the two real source locations were covered by the $CONC_{E50\%}$ in all four examples, the NNLS algorithm was not able to separate the two closely spaced plumes (Figure 3.2, 2nd column) especially for the ones with SD=2. This was because the current beam geometry has relatively coarse pixels and did not have sufficient spatial resolution to differentiate the two plumes. In spite of the high CCF_{PIC} values obtained (>0.99), the NNLS algorithm tended to merge the two small plumes into one large plume. Note that the pixel resolution was limited by the number of beam paths. On the other hand, the current beam geometry was adequate to reconstruct two plumes that were not adjacent to each other, as demonstrated in Figure 3.1. This suggests that the HRPM technique could be used as a screening tool to narrow down the area to search for the potential emission sources, rather than to map the exact spatial distributions of the plumes. In that type of application, it is not critical to separate the two plumes, and conventional point samplers could be employed in the follow-up survey to acquire more accurate source location estimation.

For the 4 cases with narrow plumes of which the NNLS failed to reconstruct both peak locations, 3 of them had one of the two reconstructed plumes located near the origin (Table 3.1, 1st row). One example of the failed reconstruction results is given in Figure 3.3a with one peak in Pixel A (i.e., near the origin) and the other in Pixel E. The CONC$_{E50\%}$ only covered one of the real source locations (in Pixel E), although the source location in Pixel A was still covered by the regions with relative concentration between 25% and 50% (Figure 3.3b). In Figure 3.3a, the low concentration detected by Paths 1 and 2 prevented the algorithm from assigning a high concentration value in Pixel A. Instead, a high concentration value was assigned in Pixel E (Figure 3.3b) to yield a high PIC for Paths 3, 5, 6 and 7, leading to biased results. We further examined the other five test maps with one of the plumes in Pixel A but with both peaks covered by CONC$_{E50\%}$. One such example is given in Figure 3.3d. Although the CONC$_{E50\%}$ covered both real sources (Figure 3.3e), its area was larger (201.5 square units, 22.4% of the studied domain) than the average value. On the other hand, this issue is less of a concern for larger plumes (Figures 3.3g and 3.3j). In both cases, the CONC$_{E50\%}$ covered both real sources (Figures 3.3h and 3.3k) and the corresponding areas (197.3 and 205.5 square units) were close to the average value. The reason of getting better results for larger plumes is that they were detected by all the beam paths in Pixel A, thus the algorithm had sufficient information to identify them successfully.

Our previous study demonstrated that the smooth basis function minimization (SBFM) algorithm is an alternative method for reconstructing plumes near the origin when only one plume existed in the studied area. In the SBFM algorithm, a known smooth basis function with unknown parameters is chosen to characterize the plume. By minimizing the error function between the observed and predicted PIC, the unknown parameters can be estimated. We applied this algorithm to reconstruct the test maps with two plumes that were both close to the origin. For the two examples of narrow plumes in Figure 3.3, the SBFM did not locate the two plumes accurately, either (Figures 3.3c and 3.3f). This is because the current beam geometry did not have sufficient segmenting information to detect these narrow plumes. In a real-world application, we can judge whether there is a narrow plume near the origin by examining the collected PIC data in detail. That is, a high PIC value detected by the short paths of the beam geometry indicates a plume near the origin.[17] Although in this case, the SBFM would work well for one plume as demonstrated in previous studies,[9] we cannot rule out the possibility of other plumes existing. In this circumstance, the beam geometry needed to be adjusted by moving the ORS instrument away from the plumes.

As discussed above, the NNLS tended to merge two adjacent plumes into one large plume (Figure 3.2). We attempted to improve the reconstruction results with two different approaches. For the test maps in Figures 3.2a and 3.2g, the SBFM algorithm revealed two plumes (Figures 3.2c and 3.2i). The uncertainty area also decreased (CONC$_{E50\%}$=32.3 and 153 vs. 186.5 and 205.5 square units from the NNLS algorithm).

When the sources were away from the origin (Figures 3.2d and 3.2j), we attempted to

incorporate the grid translation (GT) technique[29, 28] into the original NNLS algorithm to further decrease the uncertainty (i.e., area of the $CONC_{E50\%}$). The SBFM was not considered in this case because the segmenting information was very limited when the plume was away from the origin.[26, 17] Previous studies have shown that combining the conventional CT with the GT technique provides a more accurate concentration estimate than using only the CT approach.[28] In the GT technique, the pixels described in the experimental configuration were modified each time that a NNLS reconstruction was performed. In this study, the basis grid cells (i.e., pixels) were translated along the x and/or y directions by multiples of one-fifth of the width of the basis grid cell. The total number of translated grids was 25 (five times on the x-axis by five times on the y-axis). For each of the 25 translated grids, the NNLS reconstruction was implemented to estimate the concentration within each pixel. The reconstructed concentrations from these 25 grids were further interpolated by kriging to produce an overall map with a finer resolution. The results showed that adding the GT technique into the NNLS algorithm did not improve the ability of the HRPM technique to reconstruct the plumes (Figures 3.2f and 3.2l). This was because the area of several translated pixels on the edges was small and the NNLS algorithm assigned high values in those small pixels when a plume was detected by a beam path near the edges. Good results were obtained by incorporating GT into the conventional CT technique because the multiple ORS instruments and scanning beam paths formed a complicated beam geometry. This guaranteed that all pixels were passed by an adequate number of beam paths even during the translation to provide additional information for confining the possible solutions.

For the sensitivity analysis, various levels of noise were added to the PIC data. Although generally the number of failed cases increased when more random error was added as expected, this number increased to just 5 cases for the narrow plumes at the 10% level and remained as 0 for the wide plumes at the 20% level. In our own field QA/QC evaluation, the accuracy for one of the common ORS instruments, the open-path Fourier transform infrared spectrometer, was estimated to be within ±5% to ±10%. This suggests that applying the NNLS algorithm on OP-FTIR data should provide reliable results during stable weather conditions. It is worth noting that fluctuating meteorological conditions may introduce additional errors since in the real-world application the PIC data of each beam path usually are not collected simultaneously. The magnitude of this type of error could be partially reduced by calculating the moving average of the input PIC before the NNLS reconstruction, as described in the OTM-10 and Hashmonay.[10] The mean area of the $CONC_{E50\%}$ did not vary significantly at different noise levels (data not shown), indicating that the uncertainty was less affected by the added error.

To further evaluate the performance of the HRPM technique, the peak location of each plume in the test maps was shifted randomly within the original pixel of choice. This process was repeated three times for each map so 216 (3x2x36) additional test maps were generated. Among the three series test maps with wide plumes (n=36 each), 10, 7 and 6 of them did not have both peak locations

covered by the $CONC_{E50\%}$. Nonetheless, all these cases but one still had the peaks covered by the regions with relative concentration higher than 25%. On the other hand, among the three series test maps with narrow plumes (n=36 each), 9 to 13 of them had at least one peak not covered by the regions with relative concentration higher than 25%. The main reason of the poor performance on these narrow plumes is that many of them were not detected by any of the beam paths due to the shifted peak locations. Increasing the number of beam paths could solve this problem, although previous field studies suggested that plumes tended to disperse considerably.[7] Determining the optimal number of beam paths and pixel resolutions relative to the expected plume size would require further investigation.

In addition to evaluating the test maps with two plumes, we also assessed the scenarios where three plumes existed simultaneously. Several examples are given in Figure 3.4. When the plumes were away from the origin (Figures 3.4a –3.4c), the NNLS algorithm was able to locate the source locations within the region of the $CONC_{E50\%}$. Depending on whether the plumes were adjacent to or separated from each other, the NNLS algorithm reconstructed one large plume (Figure 3.4a) or several small plumes (Figures 3.4b and 3.4c), respectively. When one of the plumes was near the origin, the region of the $CONC_{E50\%}$ did not always cover all three peak locations (Figures 3.4d –3.4f), similar to the phenomenon observed for the two-plume scenarios.

One limitation of this study was using simplified Gaussian distributions to generate test maps. In real-world applications, the plumes do not necessarily have identical distributions. For example, the concentration difference between the two plumes may compromise the ability of the HRPM technique to locate the peak locations correctly. The plume with the low concentration could be 'ignored' by the algorithm because it contributes less to the collected PIC. However, identifying the major plume might be sufficient from the view of pollution control. More comprehensive studies should be conducted using both computational simulation and field experiments to further investigate how the concentration difference affects the ability of the HRPM technique to locate multiple emission sources. The issue of getting additional dispersive turbulence due to obstacles or non-flat topography[17] also should be examined.

3.3 SUMMARY

This study presented the evaluation results of the application of the HRPM technique to locate multiple plumes. The NNLS algorithm was relatively robust enough to perform in most of the simulated situations when the size of the plumes were approximately the same or larger than the geometry's resolution. This supports the use of the NNLS-HRPM methodology described in the OTM-10 of the US EPA for source locating. Although under certain situations (e.g., Figures 3.2c vs. 3.2b) the SBFM algorithm gives better results, its implementation will be problematic at solving more than two Gaussian functions (> 9 parameters to be retrieved) with the current nine-beam geometry. This simulation study also showed that for scenarios with a narrow plume near the origin

(judged from the measurements of the short beam paths), the beam geometry should be adjusted and moved away from the plume. Further field experiments should be implemented to verify the simulation results.

Table 3.1. The summary statistics of the NNLS reconstruction results for test maps with SD=2.

Locations of plumes	Successful case			Failed case	
	Number	CCF_{PIC} (mean±std)	Area of $CONC_{E50\%}$[a] (mean±std)	Number	CCF_{PIC} (mean±std)
One plume in Pixel A (inner zone from origin)	5	0.80±0.06	176.4±35.2	3	0.92±0.03
Both plumes in Pixels C, F, G, H, and I (outer zone from origin)	9	0.99±0.01	173.3±26.1	1	1.00
Both plumes in Pixels B, D, and E (middle zone from origin)	3	0.85±0.01	197.4±19.6	0	N/A
One plume in Pixels C, F, G, H, and I (outer zone) and one plume in Pixels B, D, and E (middle zone)	15	0.95±0.03	169.0±19.7	0	N/A
Overall	32	0.93±0.08	174.0±24.5	4	0.94±0.05

[a] The area of the $CONC_{E50\%}$ was only calculated for successful cases.
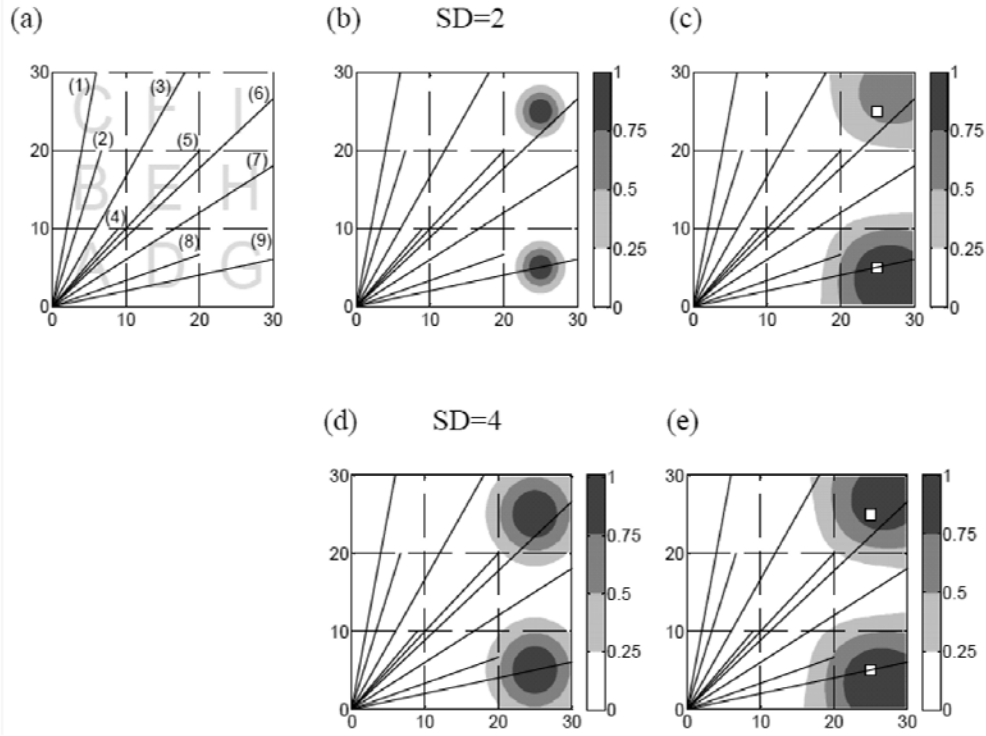
Figure 3.1. (a) The plan view of the simulated beam geometry. The letters A to I represent the pixel IDs, and the numbers in parenthesis represent the beam IDs. (b)　An example of the test map with two Gaussian distributions (SD=2). (c) The reconstruction results of (b) by the NNLS algorithm. (d) An example of the test map with two Gaussian distributions (SD=4). (e) The reconstruction results of (d) by the NNLS algorithm. The grayscale bars represent the relative concentration levels of the reconstructed plumes.
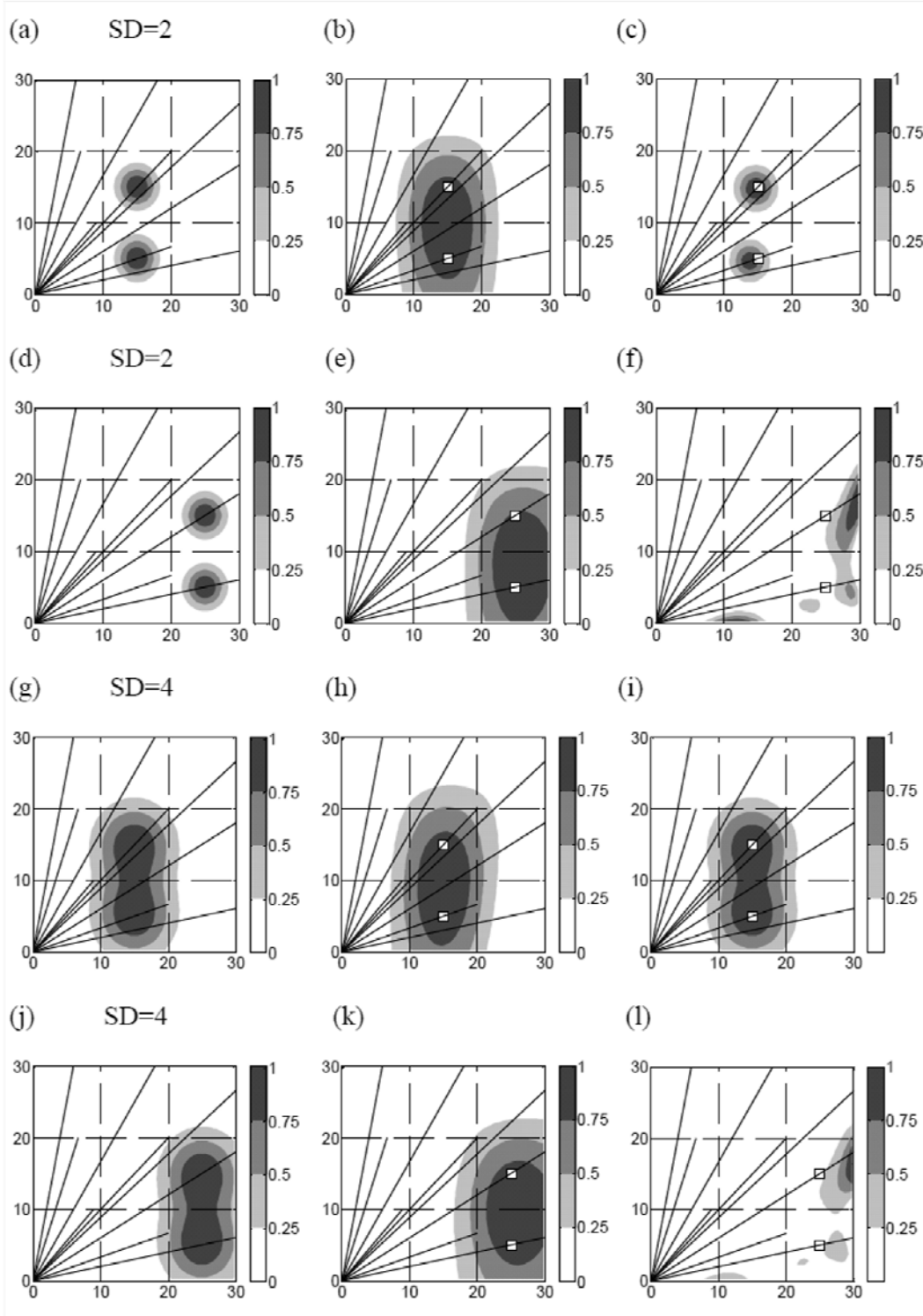
Figure 3.2. Examples of the reconstruction results for the test maps with two plumes in close proximity to each other. First column (a) (d) (g) (j): Test maps. Second column (b) (e) (h) (k): The NNLS reconstruction results. Third column (c) (i): The SBFM reconstruction results; (f) (l): The NNLS-GT reconstruction results. The white squares represent the real source locations. The grayscale bars represent the relative concentration levels of the reconstructed plumes.
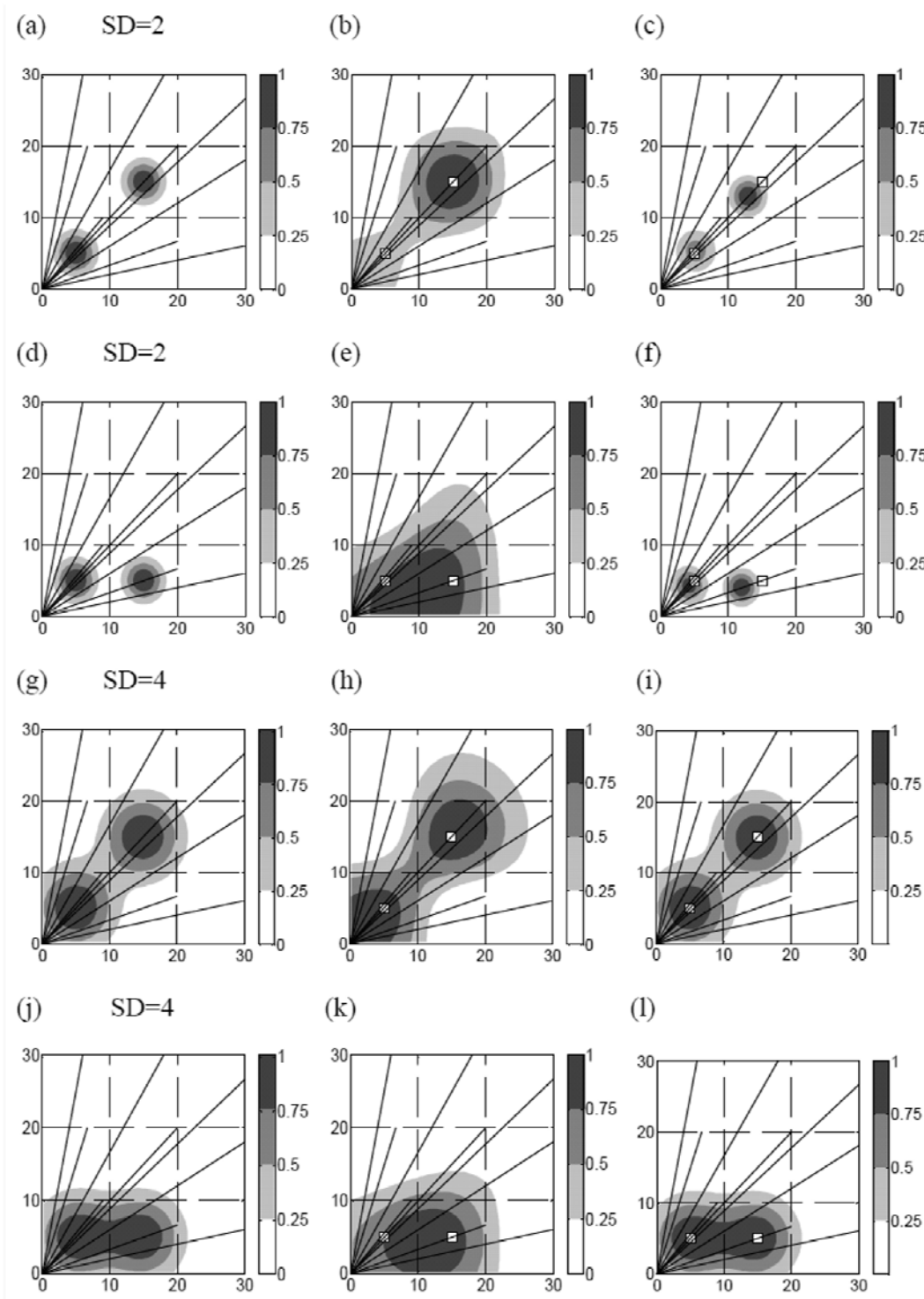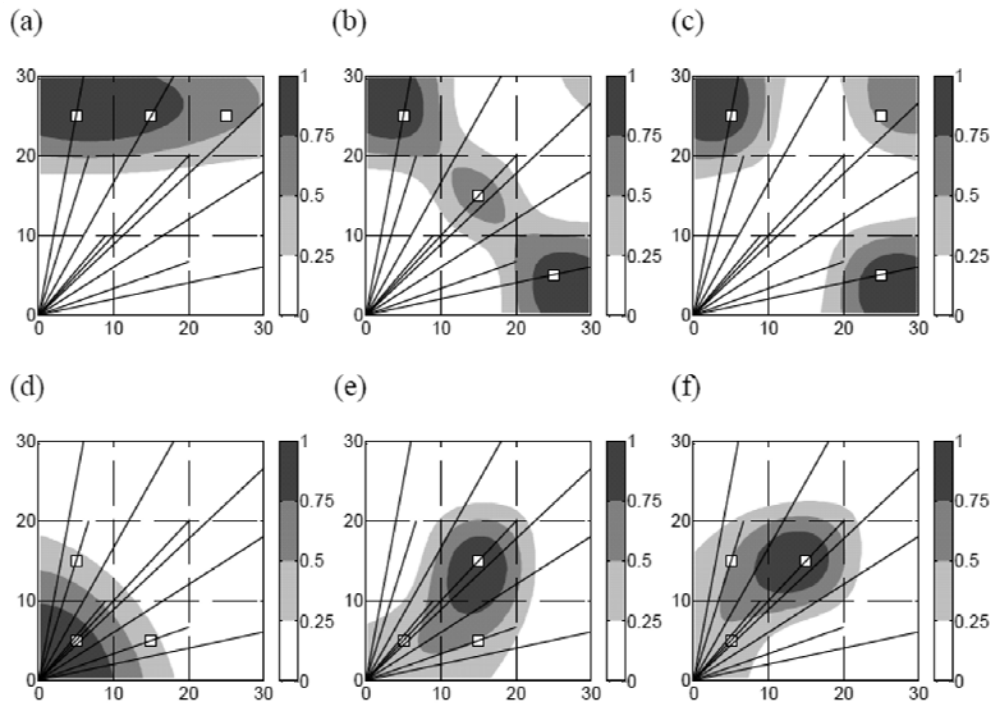
Figure 3.3. Examples of the reconstruction results from the NNLS and SBFM algorithms for test maps with one of the simulated plumes close to the origin. First column: Test map. Second column: The corresponding NNLS reconstruction results. Third column: The corresponding SBFM reconstruction results. The white square represents the real source location. The grayscale bars represent the relative concentration levels of the reconstructed plumes.

Figure 3.4. Examples of the reconstruction results for test maps with three plumes. (a) (b) (c): the plumes are away from the origin. (d) (e) (f): the plumes are close to the origin. The white squares represent the real source locations. The grayscale bars represent the relative concentration levels of the reconstructed plumes.

4. INVERSING DISPERSION MODELS

In this study, we used an open-path Fourier transform infrared spectrometer (OP-FTIR) to collect the path integrated concentration (PIC) data downwind from the sources. The advantages of applying optical remote sensing techniques included obtaining real-time data, detecting multiple VOCs simultaneously, and covering large spatial areas. By combining with the meteorological data, the source location can be reconstructed through reversing the air dispersion models.[1, 30] The objective of this study was investigating the feasibility of this technique through computational and field experiments.

4.1 METHODS

We set up three discrete monitoring lines at the downwind site of the survey area near an industrial complex in Kaohsiung, Taiwan. The field experiments were implemented with tracer gas released at a known location (Fig. 4.1). The releasing rate was set at 3.13 g/s. The distance between the source and the monitoring lines was 355, 565, and 780m, respectively (Fig. 4.1).

Before the field experiment, we conducted computational simulation study with the same setup as in the field experiment. The simulation domain was 1000×1000m, consist of our experiment area. In the simulation experiment, the US EPA ISCST3 model was used to generate the downwind concentration. The ISC3 model was a steady-state Gaussian dispersion model which can be used to simulate emissions from a wide range of sources. The input data needed for the ISCST3 model were emission source information and meteorological data. Meteorological data of temperature, relative humidity, and monitoring station pressure were retrieved from the Taiwan Data Bank of Atmospheric Research (DBAR) while the wind direction and wind speed data were measured by a weather station near the monitoring lines. The emission source information including the location of the source and the strength of the emission (i.e. the emission rate) were set as the same as the field experiment. The downwind concentration along each monitoring line with resolution of 1 m was calculated using the ISCST3 model. Consequently, the PIC data of each monitoring line were calculated by summing up the concentration value multiplied by 1m.

The source location (x, y) and the emission rate (Q) were reconstructed through inversing the ISCST3 model. The error function for minimization during the inversing process was the sum of squared errors (SSE) between the observed and predicted PIC, which is given as follows:

$$SSE = \sum_i \left(PIC_{observed,i} - PIC_{predicted,i} \right)^2 \qquad (4.1)$$

where the $PIC_{observed}$ was the measured PIC data and the $PIC_{predicted}$ was obtained from the integration of the ISC3 modeling results with unknown parameters x, y and Q. Once the SSE was minimized, the unknown parameters can be estimated and thus reconstruct the source information. The SSE minimizing process was implemented by using the built-in function "lsqnonlin" in the MATLAB

software.

The concordance correlation factor (CCF) between the observed PIC and the predicted PIC was to describe the fitness between two sets of data. The low CCF values (CCF<0.8) indicates that the reconstructed PIC did not fit the observed PIC well.[14] One factor that could affect the results was the variation of the wind speed and direction. Thus, we calculated the moving average of the measured PIC data and meteorological data for reconstruction. Furthermore, we added errors (±5°) to the wind direction data in the uncertainty analysis.

4.2 RESULTS AND DISCUSSION

Simulation

The computational simulation results showed that the reconstructed location approached to the real source locations with good CCF > 0.9 (Fig. 4.2a) when all the three monitoring lines detected the plumes. Nevertheless, if only one or two monitoring lines detected the plumes, the reconstructed location was rather far away from the real source locations (Fig. 4.2b).This was because the incomplete downwind PIC did not offer sufficient information for the SSE minimizing process.

Field experiment

In the field study, reconstruction results were excluded when CCF was smaller than 0.5. We first applied the reconstruction algorithm to the original PIC data and the reconstruction locations distributed around the tracer gas location (Fig. 4.3a). We further calculated the moving average PIC with a grouping of three cycles, but the reconstructed results were not better than the original one (Fig. 4.3b). Similar patterns were observed even when the moving average PIC were calculated based on a grouping of five cycles (Fig. 4.3c). It showed that the moving average process may not eliminate the effect from the large variation of wind directions in our study.

In the uncertainty analysis of adding errors to the wind direction measurements, the reconstructed locations of using original PIC data still clustered around the tracer gas location (Fig. 4.4a). On the other hand, the reconstructed locations with using moving average PIC based on a grouping of three or five cycles did not improve the results (Fig. 4.4b, 4.4c).

4.3 SUMMARY

In this study, we combined downwind PIC and meteorological data to reconstruct the source locations. The simulation results showed that it was necessary to have three detected PIC data to get converged solutions. The field results demonstrated that we could estimate the potential source locations, rather than pinpoint the exact locations. Detailed screening criteria were needed to improve the reconstruction results.
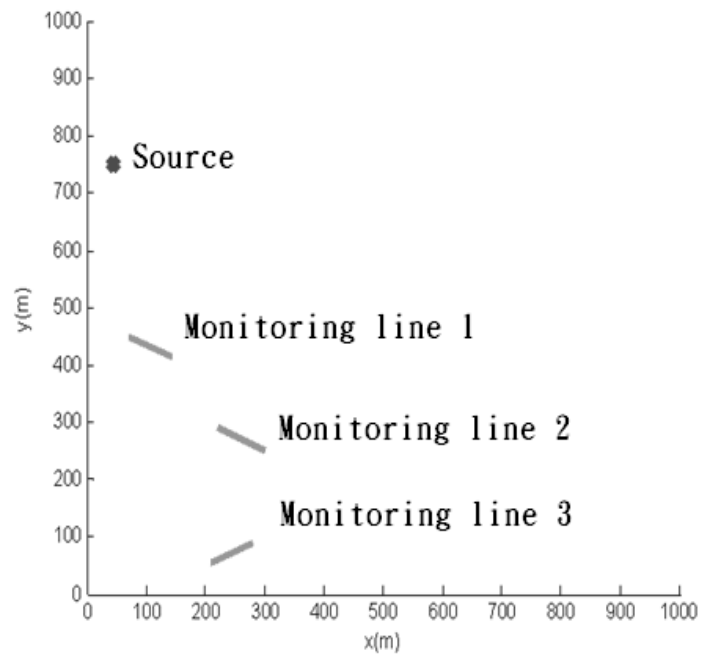
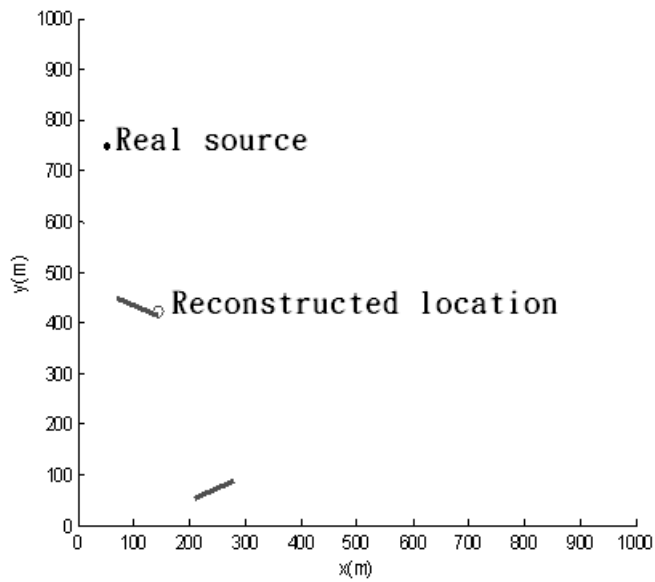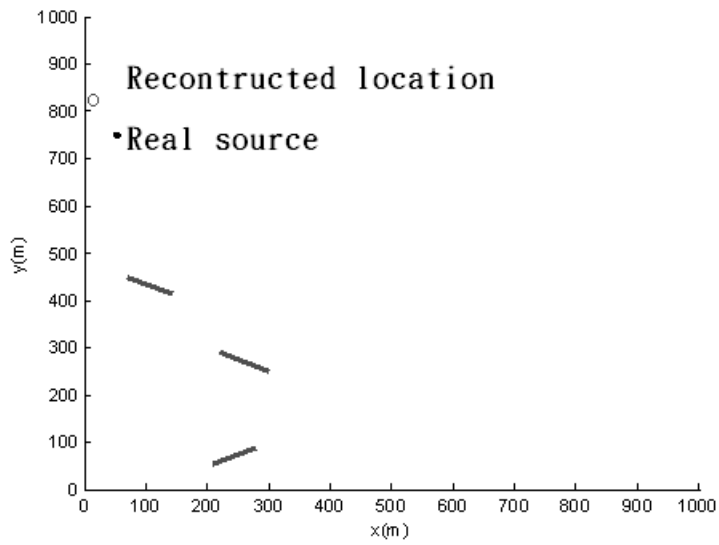Figure 4.1 The configuration of the experimental setup.

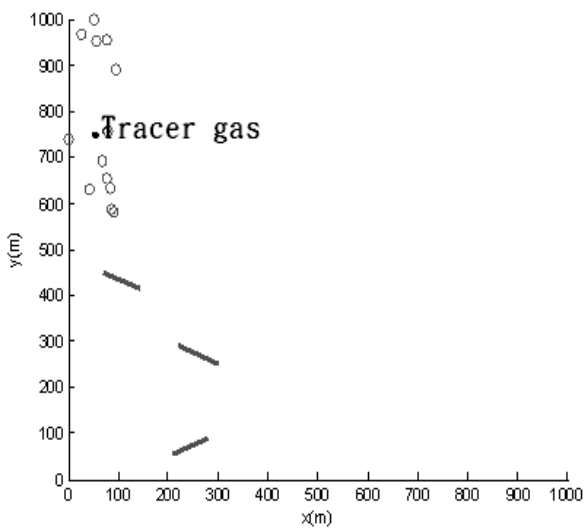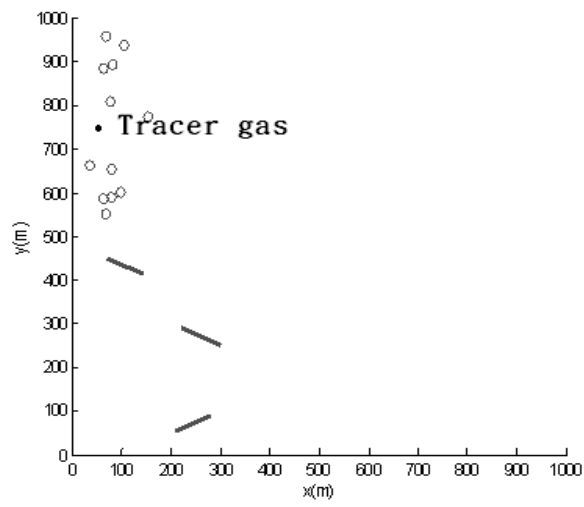Figure 4.2 The comparison between results from (a) complete PIC data and (b) incomplete PIC data.
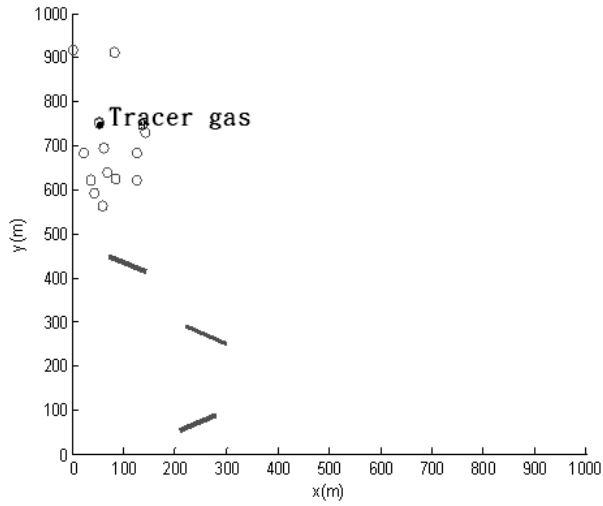
Figure 4.3 The reconstructed locations with the original PIC and moving average PIC. (a) Original (b) 3-cycle moving average (c) 5-cycle moving average
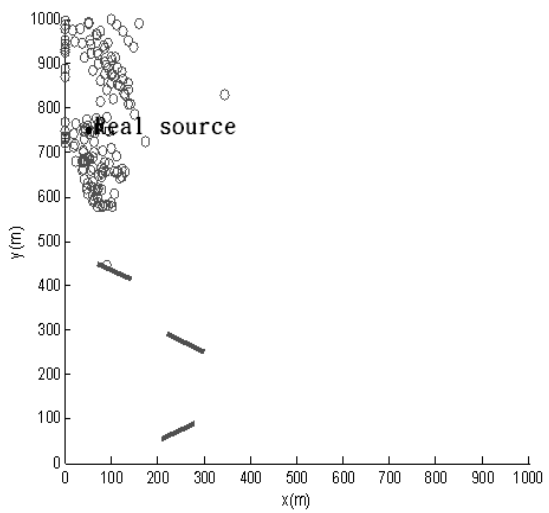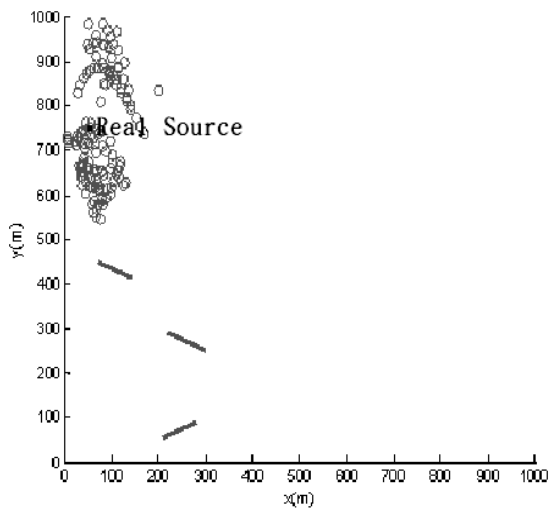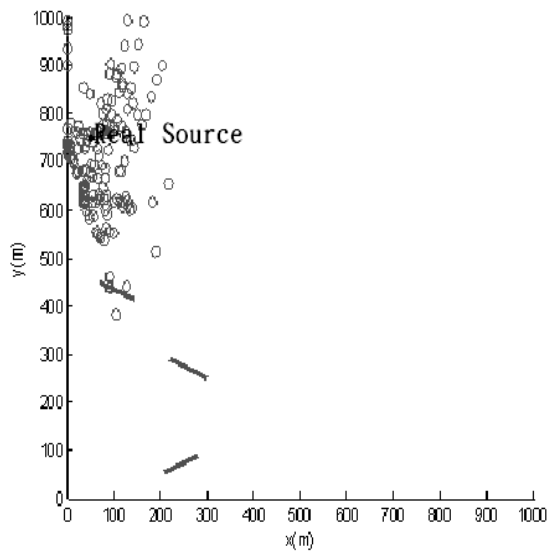
Figure 4.4 The reconstructed locations after adding errors to wind directions. (a) Original (b) 3-cycle moving average (c) 5-cycle moving average.

REFERENCES

1. Allen, C.T.; Young, G.S.; Haupt, S.E. Improving Pollutant Source Characterization by Better Estimating Wind Direction with a Genetic Algorithm; *Atmos. Environ.* **2007**, *41* (11), 2283-2289.

2. Siegell, J.H. Monitor Your Fugitive Emissions Correctly; *Chemical Engineering Progress* **1998**, *94* (11), 33-38.

3. Chen, C.L.; Fang, H.Y.; Shu, C.M. Source Location and Characterization of Volatile Organic Compound Emissions at a Petrochemical Plant in Kaohsiung, Taiwan; *J. Air Waste Manag. Assoc.* **2005**, *55* (10), 1487-1497.

4. Chen, C.L.; Fang, H.Y.; Shu, C.M. Mapping and Profile of Emission Sources for Airborne Volatile Organic Compounds from Process Regions at a Petrochemical Plant in Kaohsiung, Taiwan; *J. Air Waste Manag. Assoc.* **2006**, *56* (6), 824-833.

5. Thomson, L.C.; Hirst, B.; Gibson, G.; Gillespie, S.; Jonathan, P.; Skeldon, K.D.; Padgett, M.J. An Improved Algorithm for Locating a Gas Source Using Inverse Methods; *Atmos. Environ.* **2007**, *41* (6), 1128-1134.

6. Chen, L.Y.; Jeng, P.T.; Chang, M.W.; Yen, S.H. Rationalization of an Odor Monitoring System: A Case Study of Lin-Yuan Petrochemical Park; *Environ. Sci. Technol.* **2000**, *34* (7), 1166-1173.

7. Hashmonay, R.A.; Yost, M.G. Localizing Gaseous Fugitive Emission Sources by Combining Real- Time Optical Remote Sensing and Wind Data; *J. Air Waste Manag. Assoc.* **1999**, *49* (11), 1374-1379.

8. Burling, I.R.; Yokelson, R.J.; Griffith, D.W.T.; Johnson, T.J.; Veres, P.; Roberts, J.M.; Warneke, C.; Urbanski, S.P.; Reardon, J.; Weise, D.R., et al. Laboratory Measurements of Trace Gas Emissions from Biomass Burning of Fuel Types from the Southeastern and Southwestern United States; *Atmos. Chem. Phys.* **2010**, *10* (22), 11115-11130.

9. Fernandez-Gomez, I.; De Castro, A.J.; Guijarro, M.; Madrigal, J.; Aranda, J.M.; Diez, C.; Hernando, C.; Lopez, F. Characterization of Forest Fuels in a Mass Loss Calorimeter by Short Open-Path Ftir Spectroscopy; *J. Quant. Spectrosc. Radiat. Transfer* **2011**, *112* (3), 519-530.

10. Stutz, J.; Oh, H.J.; Whitlow, S.I.; Anderson, C.; Dibbb, J.E.; Flynn, J.H.; Rappengluck, B.; Lefer, B. Simultaneous Doas and Mist-Chamber Ic Measurements of Hono in Houston, Tx; *Atmos. Environ.* **2010**, *44* (33), 4090-4098.

11. Parsons, M.T.; Sydoryk, I.; Lim, A.; Mcintyre, T.J.; Tulip, J.; Jager, W.; Mcdonald, K.

Real-Time Monitoring of Benzene, Toluene, and P-Xylene in a Photoreaction Chamber with a Tunable Mid-Infrared Laser and Ultraviolet Differential Optical Absorption Spectroscopy; *Appl. Opt.* **2011**, *50* (4), A90-A99.

12. Sigrist, M.W., *Air Monitoring by Spectroscopic Techniques*. Wiley, New York, 1994.

13. Wu, C.F.; Chen, C.H.; Chang, S.Y.; Chang, P.E.; Shie, R.H.; Sung, L.Y.; Yang, J.C.; Su, J.W. Developing and Evaluating Techniques for Localizing Pollutant Emission Sources with Open-Path Fourier Transform Infrared Measurements and Wind Data; *J. Air Waste Manag. Assoc.* **2008**, *58* (10), 1360-1369.

14. U.S. Environmental Protection Agency. *Other Test Method 10: Optical Remote Sensing for Emission Characterization from Non-Point Sources, Research Triangle Park, NC,* 2006.

15. Turner, D.B., *Workbook of Atmospheric Dispersion Estimates : An Introduction to Dispersion Modeling*. Lewis Publishers, Boca Raton, 1994.

16. U.S. Environmental Protection Agency. *User's Guide for The Industrial Source Complex (ISC3) Dispersion Models Volume II - Description of Model Algorithms,* Research Triangle Park, NC, 1995.

17. Wu, C.F.; Chang, S.Y. Comparisons of Radial Plume Mapping Algorithms for Locating Gaseous Emission Sources; *Atmos. Environ.* **2011**, *45* (7), 1476-1482.

18. Mathworks, *Image Processing Toolbox User's Guide*. The MathWorks, Inc., Natick, MA, 2007.

19. Shonkwiler, R.W.; Mendivil, F., *Explorations in Monte Carlo Methods*. Springer Verlag, New York, 2009.

20. Byer, R.L.; Shepp, L.A. Two-Dimensional Remote Air-Pollution Monitoring Via Tomography; *Optics Letters* **1979**, *4* (3), 75-77.

21. Wolfe, D.C.; Byer, R.L. Model Studies of Laser-Absorption Computed-Tomography for Remote Air-Pollution Measurement; *Appl. Opt.* **1982**, *21* (7), 1165-1178.

22. Drescher, A.C.; Gadgil, A.J.; Price, P.N.; Nazaroff, W.W. Novel Approach for Tomographic Reconstruction of Gas Concentration Distributions in Air: Use of Smooth Basis Functions and Simulated Annealing; *Atmos. Environ.* **1996**, *30* (6), 929-940.

23. Samanta, A.; Todd, L.A. Mapping Chemicals in Air Using an Environmental Cat Scanning System: Evaluation of Algorithms; *Atmos. Environ.* **2000**, *34* (5), 699-709.

24. Hashmonay, R.A.; Yost, M.G.; Wu, C.F. Computed Tomography of Air Pollutants Using Radial Scanning Path-Integrated Optical Remote Sensing; *Atmos. Environ.* **1999**, *33* (2),

267-274.

25. Hashmonay, R.A.; Wagoner, K.; Natschke, D.F.; Harris, B.D.; Thompson, E.L., presented at the A&WMA 2002 Annual Conference Proceedings, Baltimore, MD, 2002.

26. Wu, C.F.; Yost, M.G.; Hashmonay, R.A.; Park, D.Y. Experimental Evaluation of a Radial Beam Geometry for Mapping Air Pollutants Using Optical Remote Sensing and Computed Tomography; *Atmos. Environ.* **1999**, *33* (28), 4709-4716.

27. Hashmonay, R.A. Theoretical Evaluation of a Method for Locating Gaseous Emission Hot Spots; *J. Air Waste Manag. Assoc.* **2008**, *58* (8), 1100-1106.

28. Verkruysse, W.; Todd, L.A. Novel Algorithm for Tomographic Reconstruction of Atmospheric Chemicals with Sparse Sampling; *Environ. Sci. Technol.* **2005**, *39* (7), 2247-2254.

29. Verkruysse, W.; Todd, L.A. Improved Method "Grid Translation" for Mapping Environmental Pollutants Using a Two-Dimensional Cat Scanning System; *Atmos. Environ.* **2004**, *38* (12), 1801-1809.

30. Rao, K.S. Source Estimation Methods for Atmospheric Dispersion; *Atmos. Environ.* **2007**, *41* (33), 6964-6973.